Spray-pyrolyzed Cd-substituted kesterite thin-films for photovoltaic applications: Post annealing conditions and property studies

Kelechi C. Nwambaekwe [a,b,*], Valentin P. Batir [b], Lazari Dermenji [b], Nicolai D. Curmei [b], Ernest Arushanov [b,**], Emmanuel I. Iwuoha [a,***]
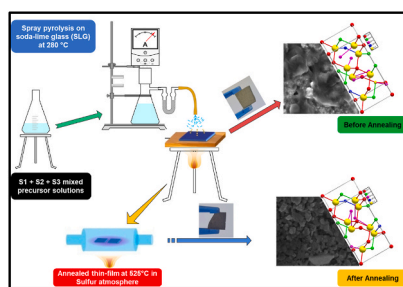
[a] NanoElectrochemistry Group, SensorLab (University of the Western Cape Sensor Laboratories), Chemical Sciences Building, University of the Western Cape, Robert Sobukwe Road, Bellville, 7535, Cape Town, South Africa
[b] Laboratory of Materials for Photovoltaics and Photonics, Institute of Applied Physics (IFA), 5 Academiei Street, MD -2028, Chisinau, Republic of Moldova

HIGHLIGHTS

- Cd-substituted kesterite thin-films were successfully prepared by spray-pyrolysis method.
- Thin-films annealed in sulfur atmosphere at 525 °C.
- Improved stoichiometry for annealed thin-films.
- Optical properties of annealed thin-films were studied and compared with unannealed thin-films.
- Crystal properties improved for annealed thin-films.

GRAPHICAL ABSTRACT

ABSTRACT

Kesterite materials were investigated for their suitability as absorber layers for thin-film photovoltaic cells. Thin-films of copper cadmium zinc tin sulfide ($Cu_2Cd_xZn_{1-x}SnS_4$) were prepared by spray pyrolysis on soda-lime glass. The obtained thin-films were subjected to post annealing treatment at 525 °C in a sulfur atmosphere to study the effects on morphology, stoichiometry, phase formation and optical properties by scanning electron microscopy (SEM), energy-dispersive X-ray spectroscopy (EDX), X-ray diffraction (XRD) and ultraviolet visible spectroscopy (UV–Vis). The XRD patterns revealed the presence of prominent kesterite peaks in the unannealed and annealed thin-films, with enhanced crystallinity in the annealed thin-films. The crystal sizes of the unannealed and annealed thin-films were estimated from the XRD data and ranged from 5 nm to 27 nm for unannealed thin-films and 13 nm–25 nm for annealed thin-films. The unannealed thin-films exhibited a non-uniformly shaped morphology, which was a mixture of cube-shaped and rod-shaped nanoparticles, while the annealed thin-films exhibited a uniformly shaped morphology of flake-shaped nanoparticles, indicating enhanced crystallinity. Chemical composition analyses revealed a divergent stoichiometry with high Cu content and deficient S content for the unannealed thin-films, while the annealed thin-films exhibited the desired stoichiometry, compensated by the sulfur atmosphere during the post-annealing treatment. The UV–Vis absorption spectra showed a high

* Corresponding author. NanoElectrochemistry Group, SensorLab (University of the Western Cape Sensor Laboratories), Chemical Sciences Building, University of the Western Cape, Robert Sobukwe Road, Bellville, 7535, Cape Town, South Africa.
** Corresponding author.
*** Corresponding author.
E-mail addresses: 3705852@myuwc.ac.za (K.C. Nwambaekwe), ernest.arushanov@ifa.md (E. Arushanov), eiwuoha@uwc.ac.za (E.I. Iwuoha).

absorption coefficient of more than 10^4 cm^{-1} for both the unannealed and annealed thin-films. The bandgap energies for the unannealed thin-films deviated from the optimum bandgap value for PV application and ranged from 2.38 eV to 1.46 eV with increasing Cd ratio, while the annealed thin-films exhibited bandgap energies of about 1.77 eV–1.28 eV with increasing Cd ratio, indicating red-shift absorption. Although other optical properties such as refractive index and dielectric properties were improved with the addition of Cd for unannealed thin-films, these properties were better in the annealed thin-films. The enhanced properties of the spray pyrolyzed Cd-substituted thin-films and their treatment after annealing can be explored as absorber layer deposition method and treatments to improve the performance and commercialization of kesterite thin-film photovoltaic devices.

1. Introduction/background

Due to the adverse effects and depletion of fossil fuels, there has recently been intensive research into alternative sustainable energy sources and materials [1–4]. Solar energy can be converted into other forms of energy using special technologies and devices, such as photovoltaic (PV) devices, which effectively convert solar energy into electrical energy [5–8]. Currently, solar cells made of multicrystalline silicon (m-Si) dominate the industry and have achieved efficiencies of more than 20%. Despite this remarkable performance, m-Si has drawbacks, such as insufficient light absorption due to the indirect band gap of 1.124 eV and the low absorption coefficient of $\sim 10^{-7}$ cm^{-1}, which requires thick absorber layers (180–200 µm), resulting in high production costs, a large amount of consumed wafer material and a high energy demand during manufacturing [9–13]. The advent of thin-film technologies has revealed alternative ways to mitigate these drawbacks. New materials have been researched, developed and used for thin-film PV cells. These new materials have properties suitable for thin-film PV applications, such as direct band gap, high absorption coefficient and low-cost method of synthesis and deposition [14–16]. Copper indium gallium sulfide/selenide (CIGS/Se) and cadmium telluride (CdTe) are good examples of the new materials adapted for PV applications. CdTe and CIGS have direct band gaps of 1.45 eV and 1.5 eV, respectively, a high absorption coefficient of $\sim 10^4$ cm^{-1} and $\sim 10^5$ cm^{-1}, and active absorber layer thicknesses of 800 nm and 2 µm, respectively [10]. They have been commercialized and have achieved PCEs of 20% for CdTe and 21.7% for CIGS [17,18]. Another disadvantage arises as they are made of elements that are not abundant, such as indium and gallium in CIGS and tellurium in CdTe, so materials have to be found that have similar properties but are made of elements that are abundant.

Copper zinc tin sulfide (CZTS), commonly referred to by its crystal structure kesterite and whose crystal structure is similar to that of CIGS (chalcopyrite), has been investigated for use in thin-film PV applications as a p-type absorber layer [19,20]. It is composed of earth abundant elements and has an optimal band gap of 1.5 eV with a large absorption coefficient of $\sim 10^4$ cm^{-1}. These properties make the material a good competitor for CIGS and CdTe devices [21]. Since its application in thin-film photovoltaics, a progressive PCE value has been achieved for the material, increasing from 0.66% as the initial PCE value to $\sim 10\%$ [10]. Sulfur was replaced in whole or in part by selenium, resulting in compounds of copper zinc tin selenide, CZTSe, and copper zinc tin sulfide selenide, CZTSSe, with PCE values of 11.6% and 12.6%, respectively. For a while, the PCE value of 12.6% from the CZTSSe solid solution was the highest reported efficiency for the material, until recently when Zhou et al. achieved a new record of 13.2% for a lithium-doped/alloyed kesterite device [22]. However, the commercialization of kesterite materials is limited because it has not attained the required PCE of 15% and is far from its theoretically calculated PCE of 35% [9]. This constraint results from the high open circuit voltage (V_{oc}) deficit of the device. The high V_{oc} deficit is attributed to a high rate of secondary phase formation, unfavorable band alignment at the p-n junction, band tail formation, and defects in the bulk [23,24]. Any deviation from the stoichiometry of the kesterite compounds leads to the formation of secondary phases, which can settle at the p-n junction of

the device, resulting in high series resistance and reduced short-circuit current density (J_{sc}) [25,26]. Antisite defects such as Cu/Zn and Sn defects lead to band tail problems that result in a mismatch between the positions of the optical and photoluminescence peaks (PL) as the PL peaks are shifted to lower energy regions [27].

With respect to these problems with the kesterite PV devices, cation substitution of the constituent elements was adopted as a strategy to solve these problems [27–29]. The use of elements with a larger atomic radius than that of the element being replaced was the main objective of the above strategy. This is the case because the proximity of the cation size and the chemical-electronic properties of Cu$^+$ and Zn^{2+} in the kesterite compound leads to the formation of Cu$_{Zn}$ and Zn$_{Cu}$ antisite defects [29]. The Cu$_{Zn}$ antisite defect leads to a reduction in the energy band gap, which adversely affects the PCE of the kesterite solar cell. Cadmium has been used to replace zinc in kesterite, leading to the formation of Cu$_{Cd}$ and Cd$_{Cu}$ antisite defects, thus reducing disorder and band tailing in kesterite compounds [30,31]. The advantageous use of Cd is due to its large ionic radius of 0.94 Å compared to Cu$^+$ and Zn^{2+}, which have an ionic radius of 0.74 Å [10,27]. Although Cd is a toxic element, its use as a substitute for Zn in kesterite compounds has yielded promising results [31,32]. In kesterite compounds with a certain ratio of Cd to Zn, the formation of the harmful ZnS has been reduced [33]. Caution should be exercised when using Cd as a substitute for Zn, since higher Cd content leads to phase transformation from the advantageous kesterite phase to the formation of the disadvantageous, less stable stannite phase. The current ratio of 40% Cd to Zn in the kesterite compound has resulted in a PCE of over 11%, with reduced band tail, as confirmed by improved band gap similarity between PL and optical measurements [31,32]. In this work, kesterite thin-films of Cu$_2$(Zn$_{1-X}$Cd$_X$)SnS$_4$ (CCZTS) were deposited by spray pyrolysis, resulting in thin-films of CZTS, copper cadmium zinc tin sulfide (CCZTS- with ratios of 20, 40, 60 and 80% Cd content) and copper cadmium tin sulfide (CCTS). To understand the effect of temperature on their properties, the thin-films were annealed in a sulfur atmosphere after deposition [34]. The crystal and phase formation of the obtained thin-films was analyzed by X-ray diffraction (XRD). The optical properties were studied by ultraviolet–visible spectroscopy (UV–Vis). The surface morphology of the thin-films was analyzed by high resolution scanning electron microscope (HRSEM). Electron-dispersive X-ray spectroscopy (EDS) provided information on the chemical composition of the thin-films.

2. Materials and Methodology

2.1. Thin-film preparation/deposition

The method of deposition involves the preparation of 3 precursor solutions (S1, S2 and S3). S1 contains Cu-complexes, S2 contains Zn- and Sn-complexes and S3 contains Cd-complexes [35]. In this way, quite stable and homogeneous (single-phase) solutions could be obtained, which can be mixed in a certain ratio just before spraying. The S1 precursor was prepared by dissolving 2.3 mg of thiourea (CS(NH$_2$)$_2$) in 17 ml of H$_2$O in the temperature range of 32–38°C with constant stirring. Then 0.83 g of CuCl was added and stirred for 3 h. To obtain the S2 precursor, 1.9 g CS(NH$_2$)$_2$ was dissolved in 17 ml H$_2$O and then 4.38 g

SnCl$_4$.5H$_2$O and 2.75 g Zn(CH$_3$COO)$_2$.2H$_2$O were added. The total volume of the solution was increased to 25 ml by adding H$_2$O. The S3 precursor solution was prepared by dissolving 1.9 g CS(NH$_2$)$_2$ and 0.4 g CdCl$_2$.2H$_2$O in 15 ml H$_2$O in the temperature range of 30–35 °C with continuous stirring. The main solution (MS) is prepared directly before the deposition. The ratio between S1, S2 and S3 is usually S1':S2 = 3:1 to obtain a stoichiometric mixture of precursors. Here, the S1′ precursor was obtained by adding a different amount of the S3 precursor to the S1 to obtain the required Cd/Zn ratio (see Table 1). The undiluted MS obtained has a concentration of 0.33 M and the MS diluted with water has a molar concentration of 0.06 M.

MS was deposited on previously cleaned transparent soda lime glass (SLG) by spray pyrolysis in a carbon dioxide atmosphere at a temperature range of 270–280 °C in a glovebox spray pyrolyzer to eliminate any oxygen interference during the formation of the kesterite thin-films. The setup of the spray pyrolyzer is shown in Scheme 1. To improve the crystalline quality of the obtained kesterite thin-films, an annealing was performed after deposition. To compensate for the lack of sulfur in the films and to prevent it from being lost during the heat treatment, a consecutive annealing was performed under S2 atmosphere at 525 °C for 30 min.

2.2. Characterization techniques

X-ray diffraction (XRD) analysis to determine the crystal phases of the deposited thin-films were performed using a Philips PW 1830 X-ray diffractometer with Cu-Kα radiation at a wavelength of 1.5406 Å (Philips, Amsterdam, The Netherlands). The software MATCH and DIAMOND (Crystal Impact, Bonn, Germany) were used to determine the lattice parameters and to simulate the crystal structure of the thin-films. Morphological and elemental analyzes of the thin-films were performed using an Auriga field emission scanning electron microscope (FESEM) equipped with an energy-dispersive X-ray spectrometer (EDXS) (Carl Zeiss Microscopy GmbH, Jena, Germany) and operated at an accelerating voltage of 200 kV. Optical studies in the wavelength range from 300 nm to 900 nm were performed using the Varian Cary 300 ultraviolet–visible–near-infrared (UV–Vis) spectrometer (Agilent, Santa Clara, CA, USA).

3. Results and discussions

3.1. Crystallographic studies

CZTS and its elementally substituted compounds occur in 3 distinctive crystal phases: Kesterite, Stannite, and wurtzite configurations. The kesterite and stannite phases exist as tetragonal configurations and show similar XRD patterns that can be distinguished only by Raman spectroscopy [36–38]. The wurtzite phase adopts a hexagonal configuration and exhibits characteristic triplet peaks of 100, 002, and 101 planes corresponding to 2θ-positions of 26.89°, 28.21°, and 30.40°, respectively [39,40]. The kesterite phase has been shown to be the most stable phase and is best suited for PV applications with characteristic XRD peaks at 2θ positions of 28.42°, 32.93°, 42.26°, and 56.07°
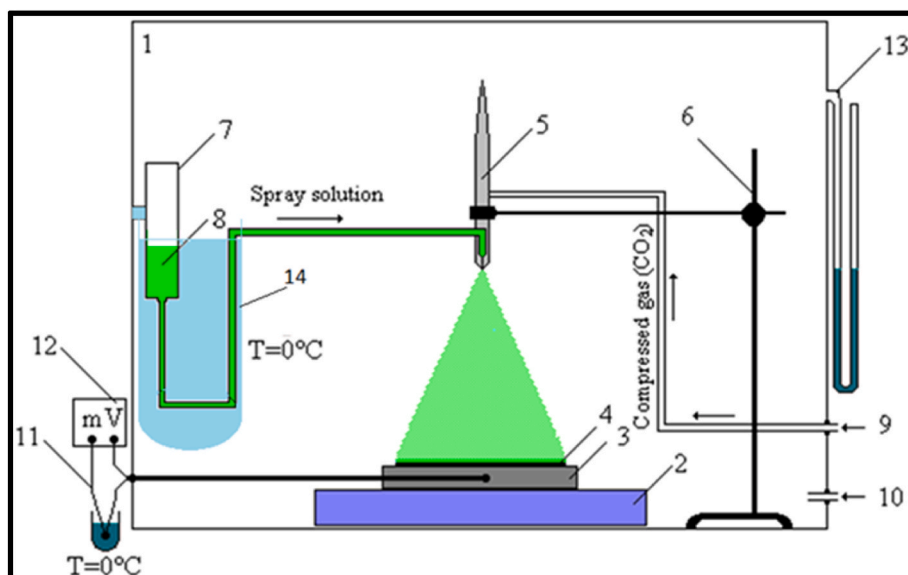
Table 1
The composition of the precursor solutions that were mixed to obtain the final solution for deposition of CCZTS solid solutions with different Cd concentrations.

Cd/(Cd + Zn) (%)	Volume S1 (ml)	Volume S2 (ml)	Volume S3 (ml)	Volume (H$_2$O) (ml)
0	6.0	2.0	–	22.0
20	6.0	1.6	2.4	20.0
40	6.0	1.2	4.8	18.0
60	6.0	0.8	7.2	16.0
80	6.0	0.4	9.6	14.0
100	6.0	–	12.0	12.0

corresponding to planes 112, 200, 220, and 312, respectively [33,38, 41]. Although the unannealed thin-films exhibited some of the characteristic kesterite peaks, their XRD peaks were of low intensity, suggesting a high content of amorphous material. The XRD patterns of the unannealed and annealed thin-films are shown in Fig. 1a and 1b, respectively. The unannealed thin-films showed low intensity peaks in the 112, 200, and 220 planes attributed to kesterite. The 312 plane of kesterite was shifted to the left in unannealed thin-films with high Cd content [42]. The amorphous nature of the peaks obtained for the unannealed thin-films indicates a high degree of secondary phase interference in the crystal structure of these thin-films (Fig. 1a) [43,44]. With increasing Cd content, the prominent kesterite peaks (corresponding to the 112, 200, 220, and 312 planes) of the unannealed thin-films shifted to lower 2θ values, indicating successful incorporation of Cd into the crystal lattice of CCZTS-20, 40, 60, 80, and CCTS due to substitution of Zn ions (atomic radius of 0.74 Å) by a larger Cd (atomic radius of 0.94 Å) [30]. The use of Cd as a substitute for Zn in kesterite reduces the likelihood of formation of some deleterious secondary phases and antisite defects that contribute to low performance of kesterite devices. The unannealed CCTS thin-films exhibited high amorphous content, indicating strong phase transformation and deformation reported for high Cd content kesterite materials [42,45]. For better yields when using Cd in kesterite, an optimized ratio of Cd to Zn is required. Some of the possible secondary phases present in the unannealed thin-films are copper (II) sulfide (CuS) with peak patterns at 2θ positions of 29.20°, 31.68°, 32.68°, 42.92°, 44.06°, 47.81°, 52.47°, 57.69°, 58.49°, 59.11°, 66.18° and 67.03° (JCPDS card # 79–2321); zinc sulfide (ZnS) with peak patterns at 2θ positions of 28.59°, 33.13°, 47.55°, 56.21°, 59.10° and 69.40° (JCPDS card # 80-0020); copper tin sulfide (CTS) with peak patterns at 2θ positions of 28.50°, 32.90°, 39.85°, 47.17°, 56.16°, 58.80° and 69.07° (JCPDS card # 089–4714) [43]. The presence of CuS is indicative of high copper content, although high copper content promotes the formation of a single-phase kesterite. The formation of a secondary ZnS phase is possible in the thin-films with high zinc content such as CZTS, CCZTS-20 and CCZTS-40. The formation of ZnS secondary phase is expected to decrease as the Cd content increases. The formation of the secondary phase CTS is expected to occur in a progressive manner for thin-films with low zinc content such as CCZTS-20, 40, 60, 80 and CCTS [43].

The thin-films annealed after deposition showed improved crystallinity (Fig. 1b) [46]. Annealing at a high temperature of 525 °C made the peaks of the annealed thin-films sharper and more intense. In the patterns obtained for the annealed thin-films, the prominent peaks assigned to the 112, 200, 220, and 312 planes of the kesterite phase were observed. The shift of the peaks in the 112, 200, 220 and 312 planes to the left becomes more evident in the annealed thin-films with increasing Cd content, indicating the incorporation of Cd atoms leading to lattice expansion of the crystal structures [47]. At lower Cd content (CCZTS-20 and 40), there was no significant variation in crystal phase as the peaks had sharp singlet peaks attributable to the kesterite phase, but the peaks at planes of 112, 200, 220, and 312 began to split into 2 in annealed thin-films of CCZTS-60, CCZTS-80, and CCTS, respectively, which can be attributed to a phase transformation from the kesterite phase to the stannite phase as well as a change in the lattice constants of these thin-films. Reports have shown that this is the case for kesterite-based material with high Cd content [47]. The improved crystallinity of the peaks of the annealed thin-films indicates the elimination of the secondary phases found in the unannealed thin-films.

We can determine the degree of crystallinity (DOC) (Equation (1)) of the unannealed and annealed thin-films by analyzing the XRD patterns of these thin-films in MATCH (a software from crystal-impact for analyzing XRD results). The number of crystalline peaks in the unannealed and annealed thin-films was determined by the software and used to determine the DOC of the thin-films. Fig. 3 shows the graph obtained for the DOC analysis of the thin-films. The parameters used for the calculation of DOC are summarized in Table 2.

Scheme 1. Schematic and flowchart of developed setup for deposition of kesterite thin-films in CO_2 atmosphere: a chemically cleaned SLG substrate -4 is placed in the Glove Box -1 on the graphite plate -3, which is mounted on the hotplate -2. The substrate is heated to the temperature of the CCZTS thin-film deposition. Differential thermocouple TXA -11 connected to the multimeter -12 is controlling the substrate temperature. The carbon dioxide gas is delivered to the Glove Box through the entrance -10, and the exit of the gas from the Glove Box is performed through the water seal -13. The CO_2 gas pressed up to 1.0–1.5 Torr is brought to the pulverizer -5, which is fixed at -6, through the entrance -9. The main solution -8 is poured in the bowl -7, from where it is brought via a pipe to the pulverizer -5. The bowl -7 is placed in the Dewar -14 at 0 °C to maintain the MS stability.
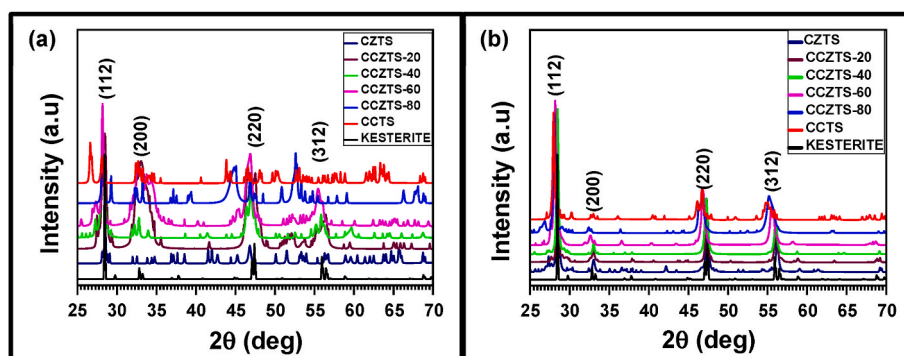

Fig. 1. Powder X-ray diffraction spectra of (a) Unannealed thin-films (b) Annealed thin-films of CZTS, CCZTS-20, CCZTS-40, CCZTS-60, CCZTS-80 and CCTS with plots of reference of kesterite phase (JCDD data file # 96-900-475).

Table 2
Parameters for calculating the DOC of the thin-films. (Parameters obtained from MATCH software analyses of XRD patterns of the thin-films).

Sample Name	Counts for Unannealed samples	Counts for Annealed samples	Total counts	DOC of Unannealed (%)	DOC of Annealed (%)
CZTS	102	553	655	15.57	84.43
CCZTS-20	154	543	697	22.09	77.91
CCZTS-40	136	612	748	18.18	81.82
CCZTS-60	149	575	724	20.58	79.42
CCZTS-80	99	554	653	15.16	84.84
CCTS	91	395	486	18.72	81.28

$$DOC = \frac{counts \text{ of samples (unannealed or annealed)}}{total \text{ counts (unannealed + annealed)}}\% \qquad (1)$$

From the DOC analysis summarized in Table 2, it appears that the addition of different Cd ratios had some effect on the crystallinity of the unannealed thin-films. With the addition of Cd, the DOC improved with slight variations in CCZTS-40 and CCZTS-80, indicating that the use of Cd affects the crystallinity of the kesterite structure [48]. The DOC for annealed thin-films improved compared to their unannealed thin-films.

The DOC of CZTS improved from 15.57% for unannealed thin-films to 84.43%, CCZTS-20 improved from 22.09% to 77.91%, CCZTS-40 improved from 18.18% to 81.82%, CCZTS-60 improved from 20.58% to 79.42%, CCZTS-80 improved from 15.16% to 84.84%, and CCTS improved from 18.72% to 81.28%. Reports have shown that annealing thin-film materials improves their crystallinity, as the high temperature ensures the removal of secondary phases or amorphous contents in the crystal structure of the materials [46].

The total broadening (β_T) of the crystal peaks is due to combined effects of broadening due to crystal size (β_D) and broadening due to lattice strain (β_ε). That is:

$$\beta_T = \beta_D + \beta_\varepsilon \qquad (2)$$

From Debye-Scherer equation, β_D is represented as:

$$\beta_D = \frac{k\lambda}{D\cos\theta} \qquad (3)$$

where k is the shape factor with value of 0.9, θ is the peak position in radians, λ is the wavelength of the source (1.5406 Å) and β_D is the full-width at half maximum (FWHM) broadening due to crystal size and D is crystal size.

And from lattice strain (ε) calculations, β_ε is calculated as:

$$\beta_\varepsilon = 4\varepsilon\tan\theta \qquad (4)$$

as ε is the lattice strain, θ is the peak position in radians and β_ε is

broadening of the peaks due to the strain. Therefore, substituting equations (3) and (4) in 2 we obtain:

$$\beta_T = \frac{k\lambda}{D\cos\theta} + 4\varepsilon\tan\theta \tag{5}$$

Equation (5) is rewritten as:

$$\beta_T\cos\theta = (4\sin\theta)\varepsilon + \frac{k\lambda}{D} \tag{6}$$

Equation (6) corresponds to a linear representation of $y = mx + c$. Plotting $\beta_T\cos\theta$ on the y-axis and $4\sin\theta$ on the x-axis gives the Williamson-Hall (W–H) representation, where the value of the slope m gives the lattice strain ε and the intercept c is equal to kλ/D, resulting in the crystal size D. Figs. 3 and 4 show the anisotropic uniform W–H deformation model for the unannealed and annealed thin-films, respectively. The analytical results are shown in Table 3.

The W–H diagrams for the unannealed and annealed thin-films, shown in Figs. 3 and 4, respectively, provide information on the uniformity and crystallinity of the 2 thin-films. Fig. 3 shows that there was no uniformity in terms of the peaks and planes used for the analysis, as the prominent kesterite peaks were not pronounced in the XRD data for the unannealed samples. The line fit shows random and divergent contact points for these material groups. This was not the case for the annealed samples. Here, the peaks corresponding to 112, 200, 220, 312 and 332 were pronounced and used in the W–H analysis (see Fig. 2b and Table 3). The line fit for all annealed samples followed the same trend, with no deviating contact points.

In determining the crystal size D, the W–H plot analysis of the thin-films revealed a trend of increasing crystal/grain size for unannealed thin-films when the Cd content was increased, with a slight variation at CCZTS-60 where the size decreased and increased again at CCZTS-80 and CCTS, respectively (Table 3). The size change indicates the successful incorporation of Cd into the crystal structure, replacing the Zn atoms [47]. It can be inferred that the addition of Cd to thin-films in varying ratios affects their crystal size. This is due to the bulkiness that the Cd additions introduce to the crystal lattice. The crystal size of annealed thin-films is larger than that of unannealed thin-films. This is because annealing allows for improved mobility and surface diffusion of the thin-films, enabling them to migrate and coalesce into larger spaces, resulting in densification and a larger crystal size. As shown in Table 3, the crystal size of CCZTS-20 increased from 6 nm to 21 nm when annealed, while CCZTS-40 increased from 12 nm to 21 nm, CCZTS-60 increased from 5 nm to 17 nm, CCZTS-80 remained the same size at 13 nm, and CCTS decreased from 25 nm to 15 nm [49].

The lattice strain (ε) of the thin-films was determined through the slope of the W–H plots, as shown in Table 3. Lattice strain is a measure of the distribution of lattice constants within a crystal and can be influenced by lattice dislocations and other imperfections in the crystal [50]. In this study, we observed that unannealed thin-films had higher lattice strain than annealed thin-films. Additionally, thin-films with lower crystal size had higher lattice strain than those with higher crystal size. The unannealed thin-film with the highest lattice strain was CCZTS-60, which had a crystal size of 5 nm and a lattice strain value of 96.1. This trend may be due to the high amorphous content in these materials. The annealed thin-films had lower lattice strain values than the unannealed

samples because their crystal sizes were larger [50,51]. The lattice strain of CCZTS-20 decreased from 82.1 in the unannealed state to 22.1 in the annealed state, while CCZTS-40 decreased from 38.2 to 21.8, CCZTS-60 decreased from 96.1 to 28.0, and CCZTS-80 decreased from 47.1 to 34.0 upon annealing. CCTS exhibited a deviation from this trend, with an increase in the lattice strain from 26.0 in the unannealed state to 32.8 in the annealed state. This deviation may be due to phase transformation and deformation caused by the high Cd content in CCTS. These results indicate that annealing at 525 °C significantly reduces the lattice strain of the thin-films. According to the W–H anisotropic uniform deformation energy density model, the number of defects at grain boundaries increases as the crystal size decreases [51]. A stress field is generated when internal pressure is exerted by the surface tension caused by volume defects. The additional stress at the grain boundaries leads to lattice strain. This may explain why the lattice strain of the annealed thin-films was significantly lower than that of the unannealed thin-films [51] (see Fig. 5a and 5b to visualize the trend between crystal size and lattice strain in the thin-films).

The dislocation density (δ), which represents the number of dislocations per unit volume of a crystalline material [51], was calculated as follows:

$$\delta = \frac{1}{D^2} \tag{7}$$

where D represents the crystal size of the samples. Crystal dislocations contribute to an increase in the lattice strain in nanostructured materials. The dislocation density in nanostructured materials provides information about the number of defects present in crystalline materials [52]. The dislocation density of the unannealed and annealed thin-films is presented in Table 3. The unannealed thin-films showed high dislocation density values, with the highest value (27.8×10^{-3} nm^{-2}) observed in CCZTS-60. This indicates that the thin-films of CCZTS-60 contained a higher volume of crystal defects compared to the other unannealed thin-films. The dislocation density of the annealed thin-films was generally lower, with the exception of CCTS, which showed a higher dislocation density than the unannealed CCTS thin-film. The reduced dislocation density in the annealed thin-films suggest an improvement in the crystal lattice, as the number of crystal defects decreased upon annealing at 525 °C.

To model the crystal structures accurately, it is necessary to determine their crystal lattice parameters. The XRD patterns obtained for the unannealed and annealed thin-films suggest that they are of the kesterite/stannite phase, which adopts a tetragonal configuration. The crystal lattice parameters a, b, and c (i.e., the lengths of the 3 edges of the crystal unit cell) and the angles α, β, and γ (the angles between the crystal unit cell edges) were evaluated for the thin-films. As all the thin-films displayed peaks attributed to the kesterite/stannite phase, the interplanar spacing (d_{hkl}) formula for tetragonal configurations was used to determine the crystal lattice parameters. In tetragonal configurations, $a = b \neq c$ and $\alpha = \beta = \gamma = 90°$. The lattice constants a, b, and c for tetragonal configurations are calculated using the following formula:

$$\frac{1}{d^2_{(hkl)}} = \frac{h^2 + k^2}{a^2} + \frac{l^2}{c^2} \tag{8}$$

Table 3
W–H analyzes parameters for unannealed and annealed thin-films of CZTS, CCZTS-20, CCZTS-40, CCZTS-60, CCZTS-80, CCTS.

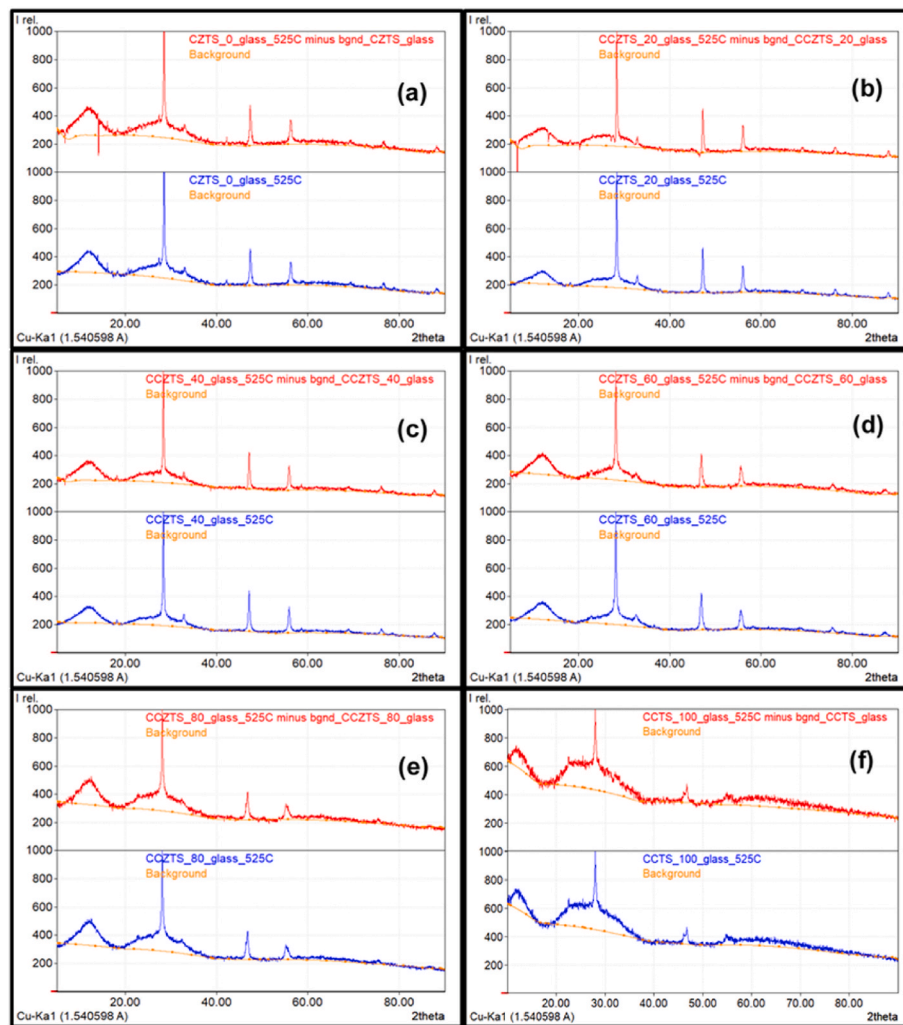| Sample	W–H Plot Analyses Unannealed Thin-films				W–H Plot Analyses Annealed Thin-films			
	β_T (10^{-3} rad)	D (nm)	ε (10^{-3})	δ (10^{-3} nm^{-2})	β_T (10^{-3} rad)	D (nm)	ε (10^{-3})	δ (10^{-3} nm^{-2})
CZTS	5.68	27	17.2	1.37	6.29	25	19.7	1.60
CCZTS-20	25.4	6	82.1	27.8	7.63	21	22.1	2.26
CCZTS-40	12.8	12	38.2	6.94	7.55	21	21.8	2.26
CCZTS-60	30.7	5	96.1	40.0	9.32	17	28.0	3.46
CCZTS-80	11.5	13	47.1	5.92	11.9	13	34.0	5.92
CCTS	6.15	25	26.0	1.60	10.3	15	32.8	4.44

Fig. 2. The graphs obtained for DOC analyses from MATCH software for (a) CZTS and CZTS@525 thin-films (b) CCZTS-20 and CCZTS-20@525 thin-films (c) CCZTS-40 and CCZTS-40@525 (d) CCZTS-60 and CCZTS-60@525 (e) CCZTS-80 and CCZTS-80@525 (f) CCTS and CCTS@525.

The lattice constants a and c can be calculated using the interplanar spacing (d-spacing) between the miller indices h, k, and l, as follows: where d_{hkl} is the d-spacing. The d-spacing value for the 220 plane (hkl) was used to calculate the lattice constant a, and the d-spacing value for the 112 plane (hkl) was used to calculate the lattice constant c. These values were obtained from MATCH software analysis of the XRD patterns. The resulting lattice constants for the thin-films are summarized in Table 4 for unannealed samples and Table 5 for annealed samples.

The d-spacing values obtained at the planes of 112 and 220 for the unannealed thin-films show an increase with increasing Cd ratio, indicating the successful incorporation of Cd into the crystal lattice of these materials. This increase in d-spacing values can also be attributed to the shift towards lower 2θ values caused by the replacement of Zn atoms (small atomic radius) with Cd atoms (larger atomic radius) [47]. The d-spacing values at the planes of 112 and 220 for the annealed thin-films also show an increasing trend with increasing Cd ratio. In terms of annealing temperature, the d-spacing values for the 112 planes decreased compared to the corresponding unannealed ratios, while the d-spacing values for the 220 planes increased relative to the corresponding unannealed ratios (see Tables 4 and 5). The lattice constants for the unannealed samples showed a decrease in the value of a with increasing Cd ratio and an increase in the value of c, with the exception of CCZTS-80 and CCTS, where c values decreased (see Table 4). The lattice constants for pristine kesterite are 5.4400 Å for a and 10.8720 Å for c, while the stannite modification has a value of 5.4550 Å for a and

10.7770 Å for c [53]. The values of a and c obtained for the unannealed and annealed thin-films correspond to those of the kesterite/stannite modifications, indicating the presence of these phases in the thin-films. The c/a ratio for the unannealed thin-films increased with increasing Cd ratio. For the annealed thin-films, the values decreased relative to the analogous unannealed ratio. The increase in the c/a ratio for the unannealed thin-films suggests elongation and expansion of the crystal lattice, which may be caused by the integration of increasing ratios of Cd atoms with a large atomic radius [54]. The expansion and elongation of the crystal lattice of the unannealed thin-films may also be due to the possible formation of secondary phases and/or deformations caused by high Cd content [55]. The lower c/a ratio observed in the annealed thin-films for concomitant ratios compared to those of the unannealed thin-films suggest contraction of the crystal lattices and an improvement in crystallinity [49]. The kesterite phase has a c/a value of 1.9990 and the stannite phase has a value of 1.9756. When comparing the c/a value of the unannealed and annealed thin-films to those of the kesterite/stannite phases, it is found that the annealed thin-films of CZTS, CCZTS-20, CCZTS-60, and CCZTS-80 have values that are more similar to the kesterite phase, while the values for CCZTS-40 and CCTS are more similar to the stannite phase [47].

The volume of the unit cell (*VUC*) for a tetragonal crystal lattice is calculated using the volume of the length, width, and height (lattice constants) of the crystal lattice and can be expressed as:
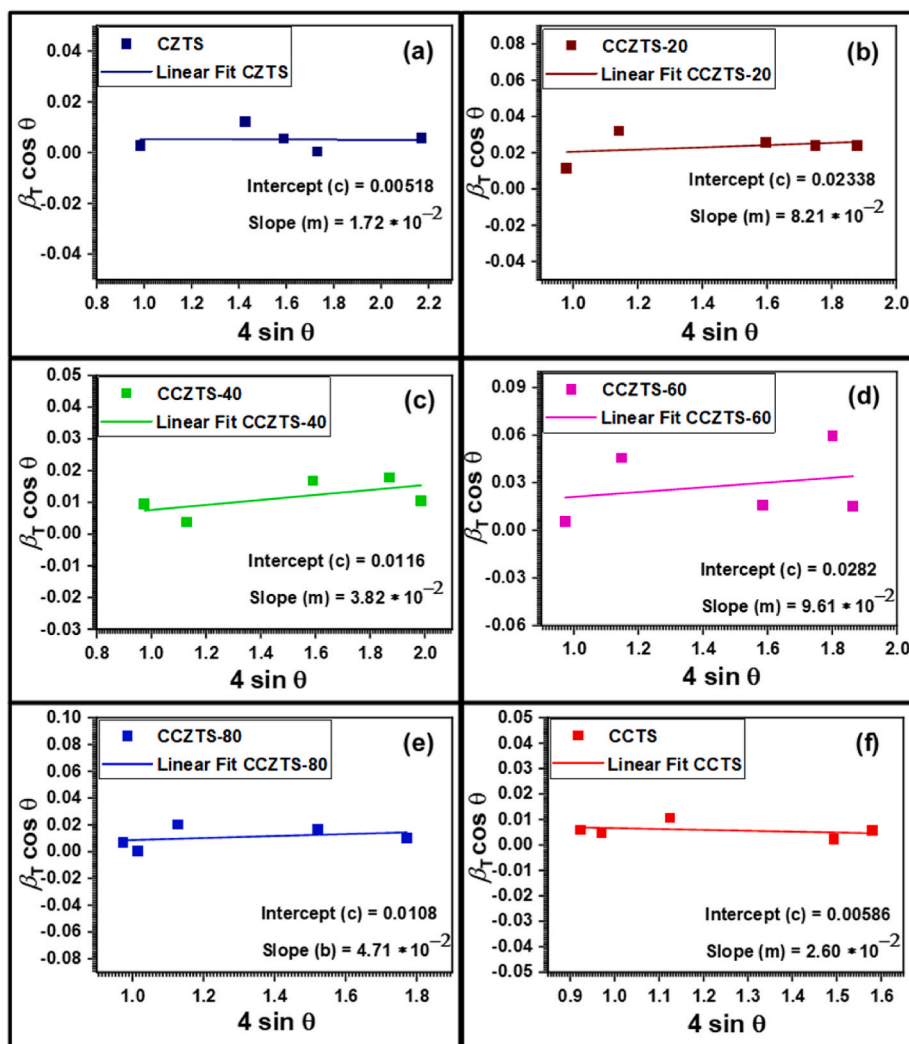
Fig. 3. W–H plot of the unannealed thin-films of (a) CZTS (b) CCZTS-20 (c) CCZTS-40 (d) CCZTS-60 (e) CCZTS-80 and (f) CCTS showing the slope and intercept values useful in obtaining the values for crystal size and crystal strain of the crystals.

$$VUC = a^2 c \tag{9}$$

In this equation, a and c are the lattice constants for the tetragonal crystal. It was observed that the VUC increased with increasing Cd ratio, which indicates expansion of the crystal lattice as more Cd was added [54]. The incorporation of Cd into the crystal lattice of the unannealed thin-films is indicated by the expansion of the unit cell as the Cd ratio increased. In contrast, the VUC for the annealed thin-films decreased relative to the corresponding unannealed ratio, indicating contraction of the unit cell. To understand the crystallography of nanostructured materials, the APF can be calculated. The APF is a measure of the volume fraction of the crystal structure occupied by its constituent particles and is a dimensionless value that is always less than one. The APF for a body-centered tetragonal crystal lattice can be calculated using the following equation:

$$APF = \frac{\pi a}{3c} \tag{10}$$

In this equation, a and c are the lattice constants. Materials with higher APF values are typically more workable, meaning that they are more ductile or malleable, because the atoms are closely packed and can easily slide over one another [52]. The APF value decreased as the Cd ratio increased in the unannealed thin-films. This indicates that as the Cd ratio increased, the crystal lattice expanded (as evidenced by the increasing VUC in the thin-films), which prevented the

atoms from being closely packed. The APF values for the annealed thin-films were higher than those of their corresponding unannealed ratios. The increase in the APF value corresponds to the decrease in the VUC in the annealed thin-films, indicating that the atoms in these films were closely packed. The high APF value supports the improved crystallinity observed in the annealed thin-films. The lattice constant values obtained from the XRD patterns of the annealed and unannealed thin-films were used to simulate the crystal structure of these materials using DIAMOND software. We simulated the crystal structures of CZTS, CCZTS-20, CCZTS-40, CCZTS-60, CCZTS-80, and CCTS for both the annealed and unannealed samples (Figs. 6 and 7). The bond lengths between the metal and sulfur, and the metal and metal are shown in Tables 6 and 7 for the unannealed and annealed thin-films, respectively. We observed that the bond lengths between the metal and sulfur increased as the Cd ratio increased in the unannealed thin-films of CZTS, CCZTS-20, CCZTS-40, CCZTS-60, CCZTS-80, and CCTS, indicating the expansion of the crystal lattice as Cd was incorporated (see Table 6). This is supported by the increasing VUC in the thin-films as the Cd ratio increased (see Table 4). The metal-to-metal bonds also increased with increasing Cd content in the unannealed thin-films. As the ratio of cadmium increased, the bond lengths between metals and sulfur (M-S) and between metals (M-M) also increased, as confirmed by the values of APF for unannealed thin-films. The APF values for these unannealed thin-films showed a decrease with increasing cadmium content, which
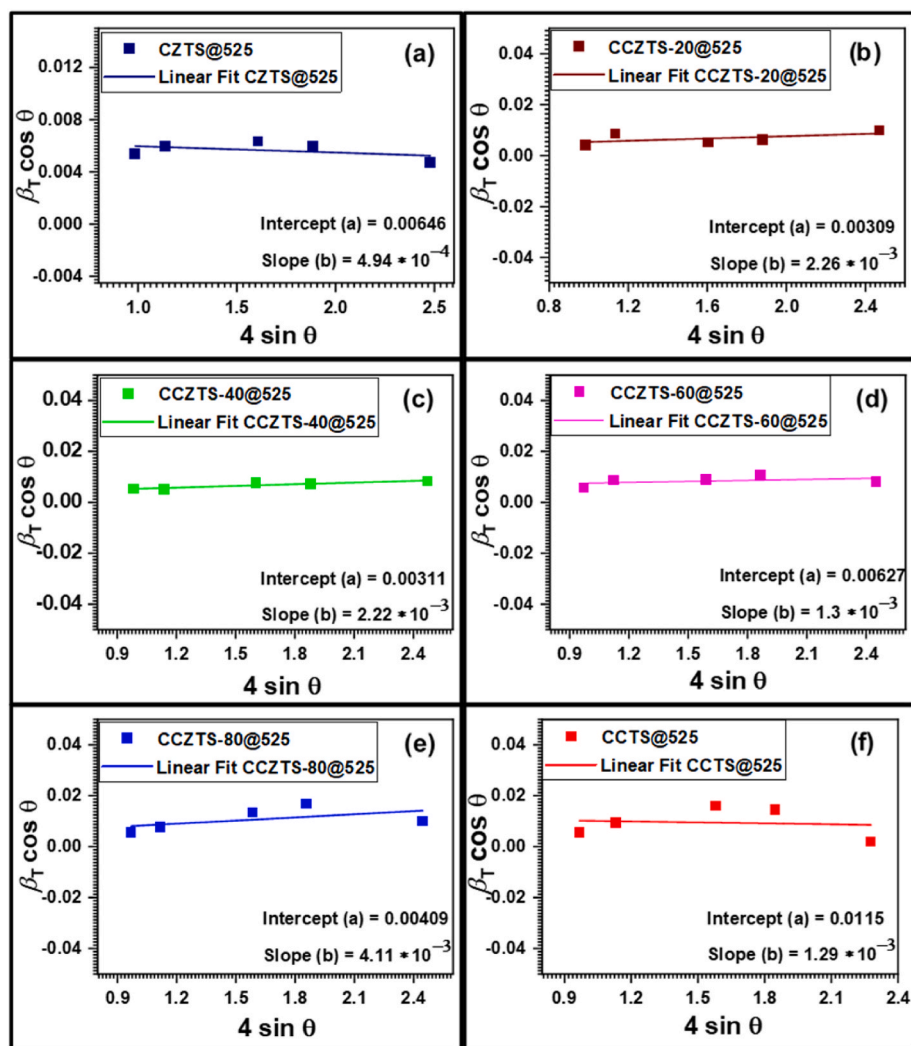
Fig. 4. W–H plot of the annealed thin-films of (a) CZTS@525 (b) CCZTS-20@525 (c) CCZTS-40@525 (d) CCZTS-60@525 (e) CCZTS-80@525 and (f) CCTS@525 showing the slope and intercept values useful in obtaining the values for crystal size and crystal strain of the crystals.
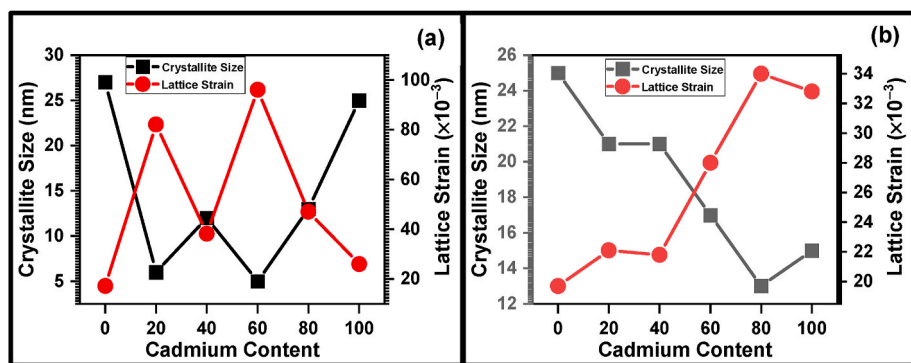

Fig. 5. Diagram of changes in crystal size and strain by W–H method for (a) Unannealed and (b) Annealed thin-films.

suggests that the atoms in these films are packed more loosely.

The M-S bonds and M-M distance in the annealed thin-films were shorter compared to their equivalent unannealed ratios (see Table 7). This indicates that the unit cell volume of the crystal lattice in the annealed thin-films is smaller. This is supported by the decreasing unit cell volume of the annealed thin-films in relation to their analogous unannealed ratio (see Table 5). The shorter M-M distance in the annealed thin-films follows the trend of the APF values in Table 5,

suggesting that the crystals in the annealed thin-films have improved workability.

3.2. Morphological and compositional studies

SEM can be used to analyze the morphology of nanoparticles. SEM micrographs provide information about the shape of the surface of synthesized materials and can give insights into grain formation when
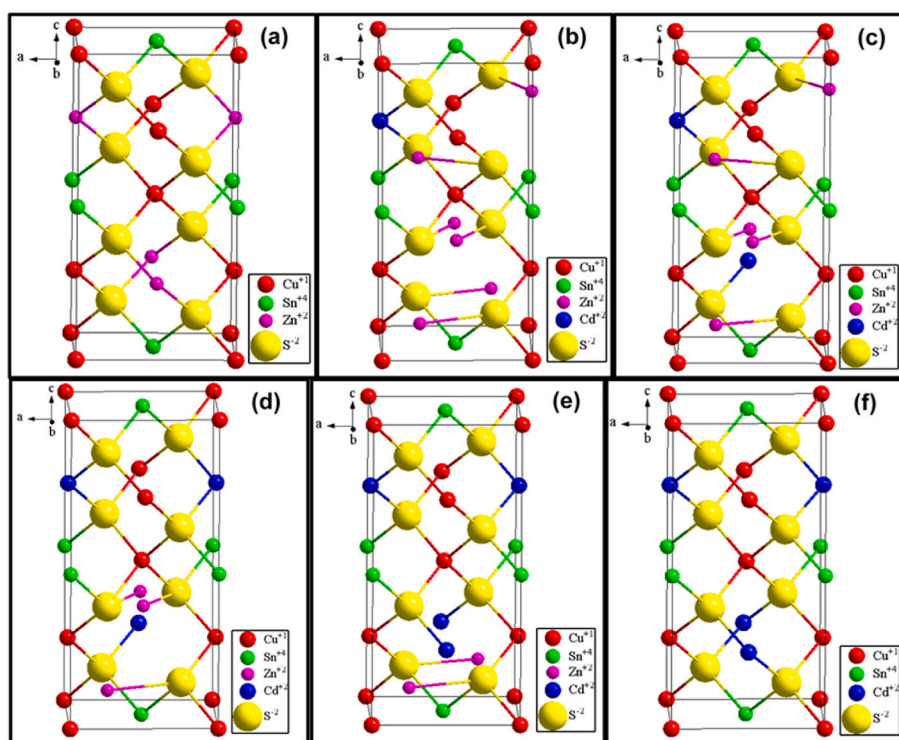
Table 4
Lattice parameter, atomic packing factor (APF) and volume of the unit cell for unannealed thin-films.

Sample	$d_{(112)}$ (Å)	$d_{(220)}$ (Å)	a (nm)	c (nm)	c/a	APF	Volume of unit cell (Å³)
CZTS	3.1420	1.9435	5.4970	10.6752	1.9420	0.5392	322.57
CCZTS-20	3.1513	1.9189	5.4274	11.0432	2.0347	0.5147	325.30
CCZTS-40	3.1599	1.9128	5.4102	11.2066	2.0714	0.5056	328.02
CCZTS-60	3.1645	1.9002	5.3746	11.4146	2.1238	0.4930	329.73
CCZTS-80	3.1556	1.9139	5.4133	11.1630	2.0621	0.5078	327.12
CCTS	3.1792	1.9353	5.4738	11.1629	2.0393	0.5135	334.47

Table 5
Lattice parameter, APF and volume of the unit cell for annealed thin-films.

Sample	$d_{(112)}$ (Å)	$d_{(220)}$ (Å)	a (Å)	c (Å)	c/a	APF	Volume of unit cell (Å³)
CZTS	3.1268	1.9155	5.4179	10.8306	1.9990	0.5239	317.92
CCZTS-20	3.1335	1.9205	5.4320	10.8470	1.9969	0.5244	320.06
CCZTS-40	3.1328	1.9216	5.4351	10.8147	1.9898	0.5263	319.47
CCZTS-60	3.1669	1.9377	5.4806	10.9930	2.0058	0.5221	330.20
CCZTS-80	3.1794	1.9407	5.4891	11.0769	2.0180	0.5189	333.75
CCTS	3.1248	1.9188	5.4271	10.7676	1.9840	0.5279	317.14

Fig. 6. Simulated crystal structures of unannealed thin-films of (a) CZTS, (b) CCZTS-20, (c) CCZTS-40, (d) CCZTS-60, (e) CCZTS-80 and (f) CCTS.

viewing cross-sections of the material. The surface morphology of the unannealed thin-films is shown in Fig. 8. In Fig. 8a, cube-like nanoparticles are seen in the CZTS thin-films. As the Cd ratio increases, rod-like particles begin to form and become more prevalent. The cube-like particles decrease in number as the Cd ratio increases, suggesting successful substitution of Cd in these thin-films. The rod-like particles are likely the result of Cd replacing Zn in the thin-films. In the case of the annealed thin-films, agglomeration of the particle shapes is observed in the CZTS (see Fig. 9a), resulting in the formation of larger grain-sized particles. The high temperature used for the annealing process eliminated the amorphous content in the thin-films, causing the particles to come together and form larger, more uniform particles due to densification. Flake-like particles become more common in the thin-films with

increasing Cd ratios (see Fig. 9b, c, d, e, and f). The high temperature improves the morphology of the thin-films by creating uniformly shaped particles with larger grain sizes, indicating improved crystallinity [49].

Energy-dispersive X-ray spectroscopy (EDX) is a useful technique for determining the chemical composition of the elements present in nanoparticles. Table 8 shows the atomic percentages of the constituent atoms in the unannealed and annealed thin-films. The unannealed thin-films showed a high content of Cu, particularly in the thin-films with low Cd content (CZTS, CCZTS-20, and CCZTS-40). There was also a low content of sulfur in all the unannealed thin-films, indicating deviation from the desired stoichiometry. This deviation may also suggest the formation of unwanted secondary phases in these samples [44]. It can be seen that the Cd atom population in the thin-films increased as expected
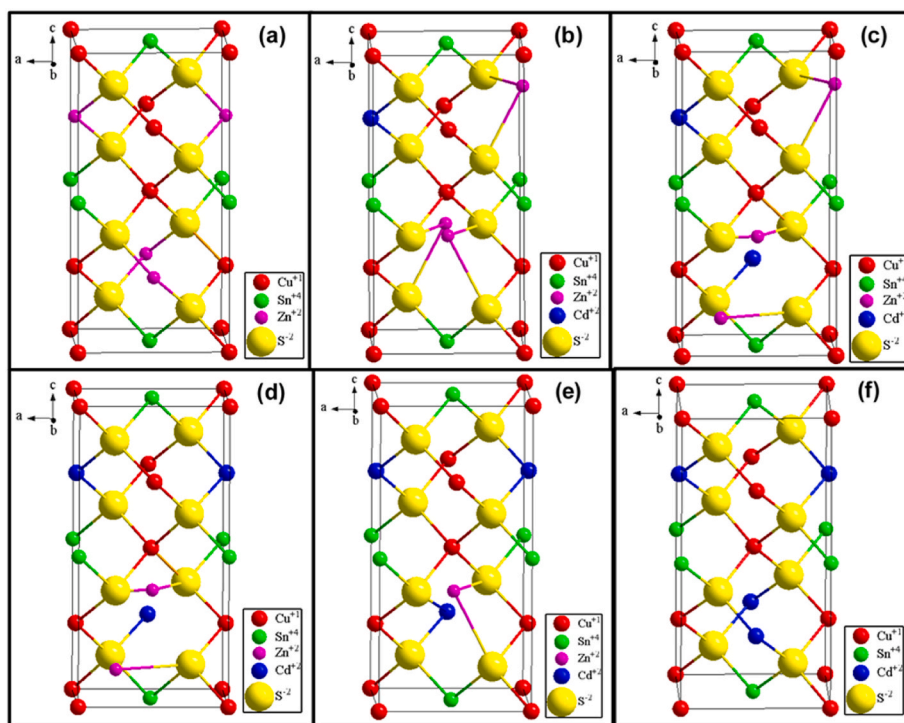
Fig. 7. Simulated crystal structures of annealed thin-films of (a) CZTS, (b) CCZTS-20, (c) CCZTS-40, (d) CCZTS-60, (e) CCZTS-80 and (f) CCTS.

Table 6
Bond-length of cation constituents with sulfur in simulated structure of unannealed thin-films (where M—M represents metal to metal distance).

SAMPLE	Cu (1)—S (Å)	Cu (2)—S (Å)	Cd–S (Å)	Zn–S (Å)	Sn–S (Å)	M—M (Å)
CZTS	2.335	2.339	–	2.343	2.415	3.887
CCZTS-20	2.343	2.345	2.348	2.988	2.421	3.871
CCZTS-40	2.351	2.351	2.355	2.978	2.428	3.895
CCZTS-60	2.358	2.356	2.360	2.959	2.434	3.920
CCZTS-80	2.349	2.349	2.353	3.044	2.426	3.888
CCTS	2.365	2.366	2.370	–	2.444	3.901
Kesterite	2.325	2.330	–	2.349	2.416	
Stannite	2.325	2.325	–	2.365	2.422	

Table 7
Bond-length of cation constituents with sulfur in simulated structure of annealed thin-films (where M—M represents metal to metal).

SAMPLE	Cu (1)—S (Å)	Cu (2)—S (Å)	Cd–S (Å)	Zn–S (Å)	Sn–S (Å)	M—M (Å)
CZTS	2.324	2.327	–	2.331	2.403	3.830
CCZTS-20	2.329	2.332	2.336	3.022	2.408	3.838
CCZTS-40	2.328	2.331	2.335	3.037	2.407	3.833
CCZTS-60	2.354	2.356	2.360	3.082	2.433	3.881
CCZTS-80	2.363	2.365	2.369	3.079	2.442	3.899
CCTS	2.322	2.325	2.329	–	2.401	3.822
Kesterite	2.325	2.330	–	2.349	2.416	
Stannite	2.325	2.325	–	2.365	2.422	

for each Cd ratio, indicating successful replacement of Zn atoms in the unannealed thin-films. The annealed thin-films showed a desirable stoichiometry, suggesting that the detrimental secondary phases were eliminated, leading to improved crystallinity of the thin-films. The low sulfur content was compensated for by the sulfur atmosphere used during the post-annealing treatment. The Cd atom population also increased with increasing Cd ratio as expected. The post-annealing treatment at 525 °C resulted in favorable outcomes, indicating that the properties of kesterite materials can be optimized at this temperature.

3.3. Optical studies

Pure CZTS and its compounds have optical properties that make them suitable as p-type absorber layers for photovoltaic applications, particularly in their kesterite phase, due to their good thermodynamic stability [10]. The kesterite phase is characterized by a high absorption coefficient (in the range of 10^4 cm^{-1} to 10^5 cm^{-1}) and an optimal energy bandgap of 1.5 eV. It is also possible to tune the energy bandgap of this material easily within the range of 1–1.8 eV through doping or replacing its constituent elements [33,56]. To study the optical properties of the deposited thin-films, ultraviolet–visible (UV–Vis) spectroscopy was used. The absorption coefficient describes the ability of a material to absorb light at a particular wavelength as it penetrates the material. It is a measure of the amount of light that can be absorbed and is typically expressed in units of inverse length, such as cm^{-1} [57]. Semiconductor materials have varying absorption coefficients, with materials that have high absorption coefficient being able to absorb more photons that can excite electrons to the conduction band. The absorption coefficient for the unannealed and annealed thin-films can be calculated from the absorbance using:

$$\alpha = 2.303\left(\frac{A}{d}\right) \tag{11}$$

Where α is the absorption coefficient in cm^{-1}, A is the absorbance, and d is the thickness of the films in nm. The thickness of the films was estimated to be around 1200 nm using a profilometer. The relation of the
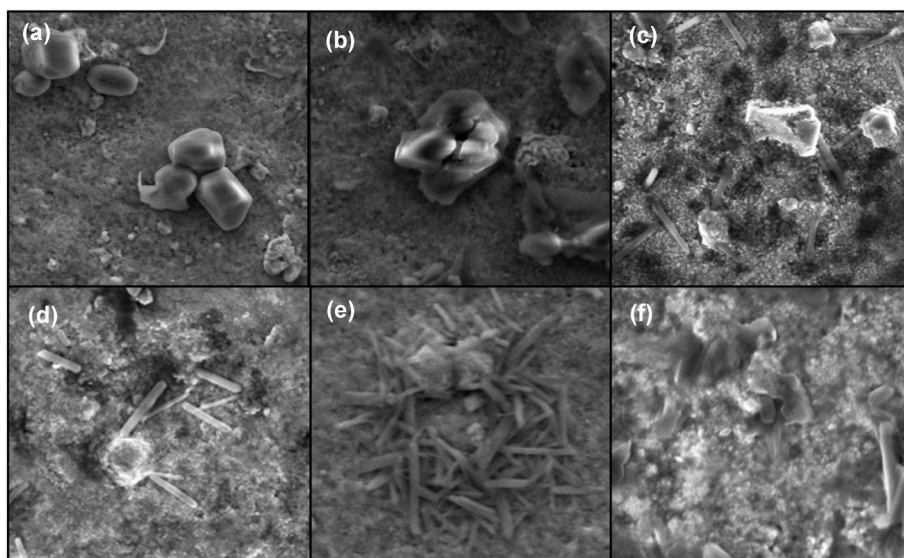
Fig. 8. SEM micrographs of unannealed thin-films of (a) CZTS, (b) CCZTS-20, (c) CCZTS-40, (d) CCZTS-60, (e) CCZTS-80 and (f) CCTS obtained at 1 μm microscopic resolution.
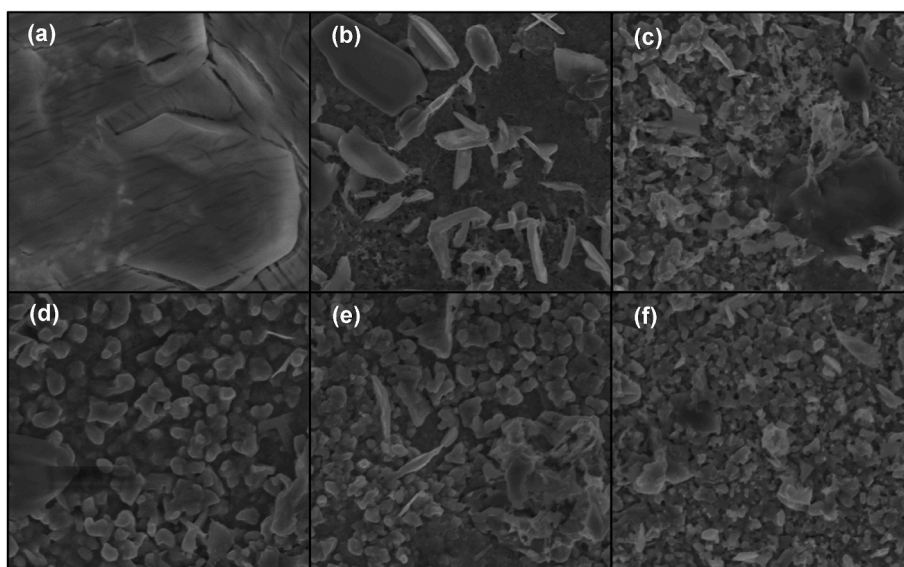

Fig. 9. SEM micrographs of annealed thin-films of (a) CZTS, (b) CCZTS-20, (c) CCZTS-40, (d) CCZTS-60, (e) CCZTS-80 and (f) CCTS obtained at 1 μm microscopic resolution.

Table 8
Chemical composition data (atomic%) for the unannealed and annealed thin-films samples.

Sample	Unannealed Thin-films					Annealed Thin-films				
	Cu	Zn	Cd	Sn	S	Cu	Zn	Cd	Sn	S
CZTS	31.71	15.74	–	17.29	35.26	21.59	14.28	–	15.8	48.33
CCZTS-20	31.44	11.43	3.23	15.1	38.79	24.42	11.47	2.53	12.76	48.82
CCZTS-40	28	11.27	4.72	16.59	39.43	23.38	9.58	3.76	13.45	49.84
CCZTS-60	27.51	6.54	8.95	17.89	39.11	22.64	5.28	8.6	14.58	48.89
CCZTS-80	27.66	4.44	12.27	20.02	35.61	22.71	3.62	9.51	15.37	48.8
CCTS	27.12	–	15.77	19.56	37.55	21.24	–	15.36	14.04	49.36

absorption coefficient to the incident wavelength for the unannealed and annealed thin-films are shown in Fig. 10a and 10b, respectively. The absorption spectra were measured within a wavelength range of 300 nm–900 nm at room temperature. It can be seen that both unannealed and annealed thin-films showed high absorption coefficient ($\sim 10^4$ cm^{-1}

ignoring reflection and transmission losses). The obtained spectra reveals that the absorption coefficient decreased with increasing incident wavelength for the unannealed and annealed thin-films but became invariant after the wavelength of 750 nm and 800 nm for unannealed and annealed thin-films, respectively. The absorption edges for the
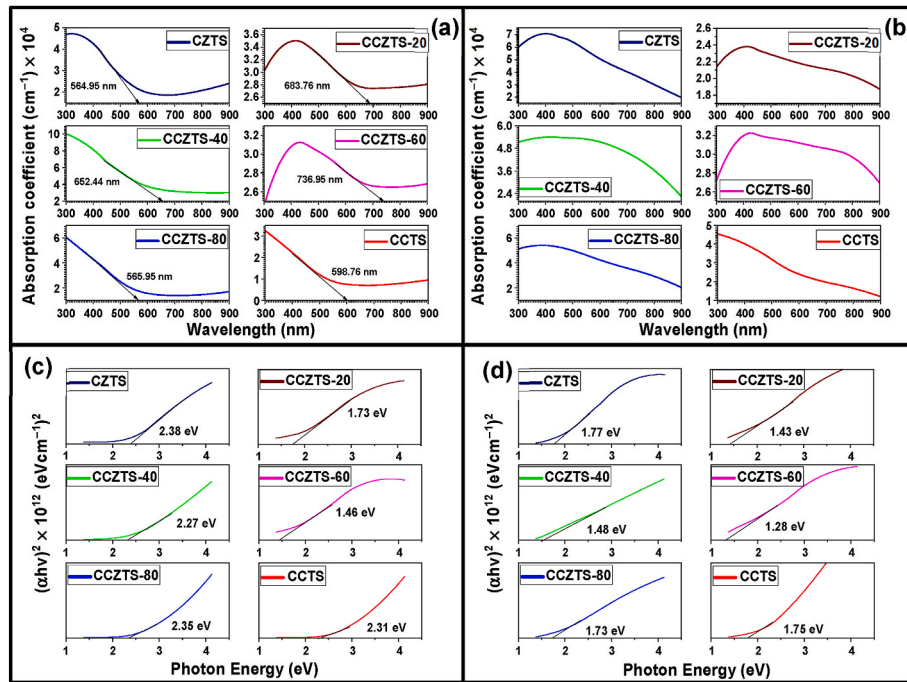
Fig. 10. UV–Vis spectra of (a) unannealed and (b) annealed thin-films; and Tauc plot showing bandgaps of (c) unannealed and (d) annealed thin-films of CZTS, CCZTS-20, CCZTS-40, CCZTS-60, CCZTS-80 and CCTS.

unannealed thin-films were obtained by extrapolating the steep position of the absorption curve to intercept at the incident wavelength axis. The absorption edge for the annealed could not be wholly determined as the thin-films displayed broad absorption across the measured incident wavelengths (see Fig. 10b). The absorption edge for all the unannealed thin-films were located at the visible region. The onsets of absorption edge for the unannealed thin-films were obtained at 564.95 nm, 683.76 nm, 652.44 nm, 736.95 nm, 565.95 nm and 598.76 nm for CZTS, CCZTS-20, CCZTS-40, CCZTS-60, CCZTS-80 and CCTS, respectively (see Fig. 10a). The onset of absorption edge for the unannealed thin-films reveals that CCZTS-60 is the optimum ratio for improved optical properties. Generally, it was observed that the addition of Cd atoms, resulted in the red-shift of the onset absorption edges of the unannealed thin-films which infers improved absorption properties of the material by the substitution of Zn with Cd [42]. The high temperature annealing at 525 °C resulted in a red-shift in the optical absorption of all the thin-films (see Fig. 10b) and broad absorption across the measurement wavelengths (300 nm–900 nm) [58,59]. Absorption maxima were observed at 398 nm, 402 nm, 405 nm, 411 nm, 413 nm, and 427 nm for CZTS, CCZTS-80, CCZTS-40, CCZTS-20, CCTS, and CCZTS-60, respectively. Red shift absorptions were observed at 726 nm, 736 nm, 591 nm, 761 nm, 756 nm, and 764 nm for CZTS, CCZTS-20, CCZTS-40, CCZTS-60, CCZTS-80, and CCTS, respectively. It is observed that high temperature annealing at 525 °C improves the optical properties of the thin-films, as seen in the red-shift absorption in the spectra shown in Fig. 10b. This is likely due to the high temperature eliminating the amorphous content in the films, leading to improved crystallinity [58].

The band gap energy (E_g) of semiconductor materials indicates the range of wavelengths in the solar spectrum that the material can absorb [51]. Kesterite materials have direct transition band gap energies that can be determined by extrapolating the linear portion of the $(\alpha h \nu)^2$ versus $h\nu$ plot, also known as the Tauc plot. The optical band gap energies of light-absorbing materials can be used to determine other optical properties of these materials, such as the refractive index and dielectric properties. The refractive index (n) of optical materials indicates how fast light travels through the material [60]. A material with a high refractive index will slow down the speed at which light travels

through it. For photovoltaic applications, an absorbing material needs to absorb a significant amount of incident light in order to generate enough electrons that can be transported through the layers of the device to achieve efficient power conversion [61]. In other words, a good semiconductor material should have a high refractive index value because the refractive index plays a significant role in determining the likelihood of total internal reflection within the solar cell [51]. The refractive index of the unannealed and annealed thin-films were studied using the Moss relation:

$$E_g n^4 = k \tag{12}$$

where k is a constant with a value of 108 eV.

The dielectric properties of a material define the ability of that material to impede the movement of electrons, resulting in polarization, when exposed to an external electric field [51]. A dielectric material is capable of establishing an electric field with minimal energy loss (ability to store energy). A dielectric material with high dielectric constant is useful to improve the performance of semiconducting devices [62]. The high-frequency dielectric constant ε_∞ of a material (which is a measure of the material's behavior at high frequencies) can be determined by the following relationship:

$$\varepsilon_\infty = n^2 \tag{13}$$

The static dielectric constant ε_o of each material (which is a measure of the material's behavior at low frequencies or static electric fields) can be obtained via:

$$\varepsilon_o = 18.52 - 3.08 E_g \tag{14}$$

The Tauc plots of band gap energies of unannealed and annealed thin-films are shown in Fig. 10c and 10d, respectively, and other derivatives of optical properties of unannealed and annealed thin-films are summarized in Table 9.

It was observed that the band gap energy of the unannealed thin-films decreased with Cd content, indicating red shift absorption caused by the replacement of Zn atoms in the thin-films by Cd atoms [63]. The bandgap values obtained for the unannealed thin-films differed from the optimal bandgap for PV devices and the values

Table 9

Estimated values of the bandgap energy (E_g), refractive index (n), high frequency dielectric constant (ε_∞) and static dielectric constant (ε_o) of unannealed and annealed thin-films.

Sample	Unannealed Thin-films				Annealed Thin-films			
	E_g (eV)	n	ε_∞	ε_o	E_g (eV)	n	ε_∞	ε_o
CZTS	2.38	2.59	6.71	11.19	1.77	2.79	7.78	13.07
CCZTS-20	1.73	2.81	7.90	13.19	1.43	2.94	8.64	14.12
CCZTS-40	2.27	2.63	6.92	11.52	1.78	2.79	7.78	13.04
CCZTS-60	1.46	2.93	8.58	14.02	1.28	3.03	9.18	14.58
CCZTS-80	2.36	2.60	6.76	11.25	1.73	2.81	7.90	13.19
CCTS	2.31	2.61	6.81	11.41	1.75	2.80	7.84	13.13

reported in literature with Cd substitution [45]. The decrease in the bandgap did not follow a definite pattern. This can be attributed to the great amount of optical incongruity due to high amorphous/secondary phases in these thin-films already explained by the XRD patterns and crystallographic analyzes of the unannealed thin-films (see Section 3.1). The high amorphous content and formation of secondary phases can be attributed to variations in the chemical composition of the material (see Section 3.2 and Table 9), which reduces the magnitude of the red shift in the absorption of these materials. Other optical properties of the thin-films, such as the refractive index and dielectric constant, improved with Cd content (see Table 9). This indicates a positive result in the substitution of Zn by Cd atoms with the best optical properties obtained for unannealed thin-film of CCZTS-60. The improvement in the optical properties of the materials with the addition of Cd suggests good applicability as a p-type absorber layer in kesterite PV devices [42]. The band gap values observed for the unannealed thin-films can be attributed to the antibonding component of s-s and s-p between the Sn cation and the S anion which can be weakened by increasing the VUC, resulting in a lower CBM and thus reducing the E_g with an addition of Cd [47]. Since other optical properties depend directly or indirectly on the optical bandgap energies of the materials, reduced bandgap values obtained with the addition of Cd atoms resulted in improved values for the other optical properties of the unannealed thin-films as reported in Table 9.

The influence of temperature on the optical properties of materials has been extensively studied [59]. The optical bandgap of the annealed thin-films improved compared to the unannealed thin-films. As previously reported in the UV–Vis spectra of the annealed thin-films, red shift absorption occurred when the thin-films were annealed (see Fig. 10b). This red shift absorption indicates reduction in the band gap of the annealed thin-films. It is worth noting that the reduction in the band gap for the annealed thin-films occurred for their successive unannealed thin film samples [42]. Improved crystallinity (see Section 3.1) and homogeneity (see Section 3.2) of the samples due to the high annealing temperature, resulted in improved optical properties of the annealed thin-films compared to their consecutive unannealed thin-films [64]. The band gap of the unannealed CZTS thin film decreased from 2.38 eV to 1.77 eV, that of CCZTS-20 from 1.73 eV to 1.43 eV, and so on (see Table 9). Since the optical band gap affects other optical properties of the materials, the redshift absorption and decreased band gap values also resulted in an improvement in the refractive index and dielectric properties of the annealed thin-films compared to their subsequent unannealed thin-films. These improvements in optical properties suggest their suitability for PV applications.

4. Conclusions

We reported the successful preparation of Cd-substituted thin-films by spray pyrolysis and investigated the effect of post annealing temperature (525 °C) on the properties of the prepared thin-films. The XRD patterns showed high amorphous content and phase deformation and transformation in unannealed thin-films with high Cd content, while the annealed films exhibited improved crystallinity, enhanced kesterite phase formation, and elimination of amorphous content, as evidenced by distinct characteristic kesterite peaks in planes of 112, 200, 220, and 312. The particle size of the materials increased upon annealing, which can be attributed to significant grain formation as amorphous content is eliminated. EDX studies of the chemical composition of the unannealed thin-films revealed a stoichiometry that was rich in Cu and sulfur poor which have been investigated to be detrimental to the PV device due to the strong formation of antisite defects. For the annealed thin-films, a desirable stoichiometry was achieved and the sulfur loss was compensated by a sulfur atmosphere during annealing. SEM Images of the unannealed thin-films showed a non-uniformly shaped mixture of cubic and rod-shaped nanoparticles. With increasing Cd content in the unannealed thin-films, rod-shaped nanoparticles were observed, indicating successful replacement of Zn atoms with Cd atoms. The morphology of the annealed thin-films showed uniformly shaped nanoparticles that increased with increasing Cd content. The UV–Vis spectra showed a decreasing band gap for the annealed thin-films due to the red shift of absorption caused by the elimination of the amorphous components. The analysis of other optical properties such as refractive index and dielectric properties showed improved values for the annealed thin-films with optimum optical properties obtained for CCZTS-60 thin-film. Notable improvements such as increased crystallinity and improved optical properties were obtained in this work by post annealing at 525 °C, which can lead to efficient fabrication output. Further work will focus on thin film PV device fabrication using the post-annealing parameters to achieve improved device efficiencies.

CRediT authorship contribution statement

Kelechi C. Nwambaekwe: Data curation, Software, Investigation, Validation, and, Writing – original draft. **Valentin P. Batir:** Visualization, Methodology, and. **Lazari Dermenji:** Visualization, Methodology. **Nicolai D. Curmei:** Visualization, Methodology. **Ernest Arushanov:** Conceptualization, Supervision, Writing – review & editing. **Emmanuel I. Iwuoha:** Conceptualization, Supervision, Software, Investigation, Validation, Writing – review & editing.

Declaration of competing interest

The authors declare that they have no known competing financial interests or personal relationships that could have appeared to influence the work reported in this paper.

Data availability

Data will be made available on request.

Abbreviations

CZTS	Copper zinc tin sulfide
CCZTS-20	Copper cadmium zinc tin sulfide-20
CCZTS-40	Copper cadmium zinc tin sulfide-40
CCZTS-60	Copper cadmium zinc tin sulfide-60
CCZTS-80	Copper cadmium zinc tin sulfide-80
CCTS	Copper cadmium tin sulfide
PV	Photovoltaic

References

[1] P.A. Owusu, S. Asumadu-Sarkodie, A review of renewable energy sources, sustainability issues and climate change mitigation, Cogent Eng 3 (2016), 1167990, https://doi.org/10.1080/23311916.2016.1167990.

[2] D. Lasrado, S. Ahankari, K. Kar, Nanocellulose-based polymer composites for energy applications—a review, J. Appl. Polym. Sci. (2020), https://doi.org/10.1002/app.48959.

[3] D. Larcher, J.M. Tarascon, Towards greener and more sustainable batteries for electrical energy storage, Nat. Chem. (2015), https://doi.org/10.1038/nchem.2085.

[4] F.J. Lozano, R. Lozano, P. Freire, C. Jiménez-Gonzalez, T. Sakao, M.G. Ortiz, A. Trianni, A. Carpenter, T. Viveros, New perspectives for green and sustainable chemistry and engineering: approaches from sustainable resource and energy use, management, and transformation, J. Clean. Prod. (2018), https://doi.org/10.1016/j.jclepro.2017.10.145.

[5] N. Kannan, D. Vakeesan, Solar energy for future world: - a review, Renew. Sustain. Energy Rev. 62 (2016) 1092–1105, https://doi.org/10.1016/j.rser.2016.05.022.

[6] L. El Chaar, L.A. Lamont, N. El Zein, Review of photovoltaic technologies, Renew. Sustain. Energy Rev. (2011), https://doi.org/10.1016/j.rser.2011.01.004.

[7] C. Wadia, A.P. Alivisatos, D.M. Kammen, Materials availability expands the opportunity for large-scale photovoltaics deployment, Environ. Sci. Technol. 43 (2009) 2072–2077, https://doi.org/10.1021/es8019534.

[8] M. El Yadari, L. Bahmad, A. El Kenz, A. Benyoussef, Monte Carlo study of the double perovskite nano Sr2VMoO 6, J. Alloys Compd. 579 (2013) 86–91, https://doi.org/10.1016/j.jallcom.2013.01.158.

[9] S. Giraldo, Z. Jehl, M. Placidi, V. Izquierdo-Roca, A. Pérez-Rodríguez, E. Saucedo, Progress and perspectives of thin film kesterite photovoltaic technology: a critical review, Adv. Mater. 31 (2019), 1806692, https://doi.org/10.1002/adma.201806692.

[10] K.C. Nwambaekwe, V. John-Denk, S.F. Douman, P. Mathumba, S.T. Yussuf, O. V. Uhuo, P.I. Ekwere, E.I. Iwuoha, Crystal engineering and thin-film deposition strategies towards improving the performance of kesterite photovoltaic cell, J. Mater. Res. Technol. 12 (2021) 1252–1287, https://doi.org/10.1016/j.jmrt.2021.03.047.

[11] C. Battaglia, A. Cuevas, S. De Wolf, High-efficiency crystalline silicon solar cells: status and perspectives, Energy Environ. Sci. 9 (2016) 1552–1576, https://doi.org/10.1039/c5ee03380b.

[12] M.A. Green, The path to 25% silicon solar cell efficiency: history of silicon cell evolution, Prog. Photovoltaics Res. Appl. (2009), https://doi.org/10.1002/pip.892.

[13] F. Ferrazza, Crystalline Silicon: Manufacture and Properties, third ed., Elsevier Ltd, 2017 https://doi.org/10.1016/B978-0-12-809921-6.00004-5.

[14] P. Vasekar, T. Dhakal, S. P, P. T, Thin film solar cells using earth-abundant materials, in: Sol. Cells - Res. Appl. Perspect., InTech, 2013, https://doi.org/10.5772/51734.

[15] K.L. Chopra, P.D. Paulson, V. Dutta, Thin-film solar cells: an overview, Prog. Photovoltaics Res. Appl. (2004), https://doi.org/10.1002/pip.541.

[16] S. Idrissi, S. Ziti, H. Labrim, L. Bahmad, Band gaps of the solar perovskites photovoltaic CsXCl3 (X=Sn, Pb or Ge), Mater. Sci. Semicond. Process. 122 (2021), 105484, https://doi.org/10.1016/j.mssp.2020.105484.

[17] P. Jackson, D. Hariskos, E. Lotter, S. Paetel, R. Wuerz, R. Menner, W. Wischmann, M. Powalla, New world record efficiency for Cu(In,Ga)Se2 thin-film solar cells beyond 20, Prog. Photovoltaics Res. Appl. 19 (2011) 894–897, https://doi.org/10.1002/pip.1078.

[18] S.K. Wallace, D.B. Mitzi, A. Walsh, The steady rise of kesterite solar cells, ACS Energy Lett. 2 (2017) 776–779, https://doi.org/10.1021/acsenergylett.7b00131.

[19] H. Katagiri, Cu2ZnSnS4 thin film solar cells, in: Thin Solid Films, 2005, https://doi.org/10.1016/j.tsf.2004.11.024.

[20] N. Saber, Z. Fadil, A. Mhirech, B. Kabouchi, L. Bahmad, W.O. Benomar, Magnetic behaviors of the kesterite and the stannite nanostructures: Monte Carlo study, Spin 12 (2022), https://doi.org/10.1142/S2010324722500084.

[21] A. Khare, Y. Li, B.S. Tosun, D.J. Norris, E.S. Aydil, Copper zinc tin sulfide solar cells, in: 11AIChE - 2011 AIChE Annu. Meet. Conf. Proc., 2011.

[22] J. Zhou, X. Xu, B. Duan, H. Wu, J. Shi, Y. Luo, D. Li, Q. Meng, Regulating crystal growth via organic lithium salt additive for efficient Kesterite solar cells, Nano Energy 89 (2021), 106405, https://doi.org/10.1016/j.nanoen.2021.106405.

[23] T. Gershon, Y.S. Lee, P. Antunez, R. Mankad, S. Singh, D. Bishop, O. Gunawan, M. Hopstaken, R. Haight, Photovoltaic materials and devices based on the alloyed kesterite absorber (AgxCu1-x)2ZnSnSe4, Adv. Energy Mater. 6 (2016) 1–7, https://doi.org/10.1002/aenm.201502468.

[24] T. Gokmen, O. Gunawan, T.K. Todorov, D.B. Mitzi, Band tailing and efficiency limitation in kesterite solar cells, Appl, Phys. Lett. 103 (2013), https://doi.org/10.1063/1.4820250.

[25] S. Giraldo, M. Placidi, E. Saucedo, Kesterite: new progress toward earth-abundant thin-film photovoltaic, in: Adv. Micro- Nanomater. Photovoltaics, Elsevier, 2019, pp. 93–120, https://doi.org/10.1016/B978-0-12-814501-2.00005-0.

[26] A. Polizzotti, I.L. Repins, R. Noufi, S.H. Wei, D.B. Mitzi, The state and future prospects of kesterite photovoltaics, Energy Environ. Sci. (2013), https://doi.org/10.1039/c3ee41781f.

[27] J. Li, D. Wang, X. Li, Y. Zeng, Y. Zhang, L. Jianjun, W. Dongxiao, L. Xiuling, Z. Yu, Z. Yi, Cation substitution in earth-abundant kesterite photovoltaic materials, Adv. Sci. 5 (2018), 1700744, https://doi.org/10.1002/advs.201700744.

[28] A.S. Nazligul, M. Wang, K.L. Choy, Recent development in earth-abundant kesterite materials and their applications, Sustain 12 (2020) 5138, https://doi.org/10.3390/su12125138.

[29] S. Bourdais, C. Choné, B. Delatouche, A. Jacob, G. Larramona, C. Moisan, A. Lafond, F. Donatini, G. Rey, S. Siebentritt, A. Walsh, G. Dennler, Is the Cu/Zn disorder the main culprit for the voltage deficit in kesterite solar cells? Adv. Energy Mater. 6 (2016) 1–21, https://doi.org/10.1002/aenm.201502276.

[30] J. Fu, Q. Tian, Z. Zhou, D. Kou, Y. Meng, W. Zhou, S. Wu, Improving the performance of solution-processed Cu 2 ZnSn(S,Se) 4 photovoltaic materials by Cd 2+ substitution, Chem. Mater. 28 (2016) 5821–5828, https://doi.org/10.1021/acs.chemmater.6b02111.

[31] C. Yan, K.K.K. Sun, J. Huang, S. Johnston, F. Liu, B.P. Veettil, K.K.K. Sun, A. Pu, F. Zhou, J.A. Stride, M.A. Green, X. Hao, Beyond 11% efficient sulfide kesterite Cu 2 Zn x Cd 1-x SnS 4 solar cell: effects of cadmium alloying, ACS Energy Lett. 2 (2017) 930–936, https://doi.org/10.1021/acsenergylett.7b00129.

[32] R. Sun, D. Zhuang, M. Zhao, Q. Gong, M. Scarpulla, Y. Wei, G. Ren, Y. Wu, Beyond 11% efficient Cu2ZnSn(Se,S)4 thin film solar cells by cadmium alloying, Sol. Energy Mater. Sol. Cells 174 (2018) 494–498, https://doi.org/10.1016/j.solmat.2017.09.043.

[33] Y.E. Romanyuk, S.G. Haass, S. Giraldo, M. Placidi, D. Tiwari, D.J. Fermin, X. Hao, H. Xin, T. Schnabel, M. Kauk-Kuusik, P. Pistor, S. Lie, L.H. Wong, Doping and alloying of kesterites, J. Phys. Energy. 1 (2019), 044004, https://doi.org/10.1088/2515-7655/ab23bc.

[34] L. Dermenji, N. Curmei, M. Guc, G. Gurieva, M. Rusu, V. Fedorov, L. Bruc, D. Sherban, S. Schorr, A. Simashkevich, E. Arushanov, Effects of annealing on elemental composition and quality of CZTSSe thin films obtained by spray pyrolysis, Surf. Eng. Appl. Electrochem. (2016), https://doi.org/10.3103/S1068375516060041.

[35] L. Dermenji, M. Guc, G. Gurieva, T. Dittrich, J. Rappich, N. Curmei, L. Bruc, D. A. Sherban, A.V. Simashkevich, S. Schorr, E. Arushanov, Thin films of (AgxCu1−x) 2ZnSn(S,Se)4 (x = 0.05–0.20) prepared by spray pyrolysis, Thin Solid Films (2019) 690, https://doi.org/10.1016/j.tsf.2019.137532.

[36] A. Zakutayev, Brief review of emerging photovoltaic absorbers, Curr. Opin. Green Sustain. Chem. 4 (2017) 8–15, https://doi.org/10.1016/j.cogsc.2017.01.002.

[37] S. Siebentritt, S. Schorr, Kesterites-a challenging material for solar cells, Prog. Photovoltaics Res. Appl. 20 (2012) 512–519, https://doi.org/10.1002/pip.2156.

[38] K.C. Nwambaekwe, M. Masikini, P. Mathumba, M.E. Ramoroka, S. Duoman, V. S. John-Denk, E.I. Iwuoha, Electronics of anion hot injection-synthesized Te-functionalized kesterite nanomaterial, Nanomaterials 11 (2021) 794, https://doi.org/10.3390/nano11030794.

[39] K. Yu, E.A. Carter, A strategy to stabilize kesterite CZTS for high-performance solar cells, Chem. Mater. 27 (2015) 2920–2927, https://doi.org/10.1021/acs.chemmater.5b00172.

[40] T. Ajjammouri, S. Aazou, O. Mahboub, Z. Laghfour, M. Bouzbib, M. Abd-Lefdil, A. Ulyashin, A. Slaoui, Z. Sekkat, Kesterite/wurtzite Cu2ZnSnSnS4 nanocrystals: synthesis and characterization for PV applications, in: Proc. 2016 Int. Renew. Sustain. Energy Conf. IRSEC 2016, IEEE, 2017, pp. 797–801, https://doi.org/10.1109/IRSEC.2016.7983993.

[41] S. Chen, X.G. Gong, A. Walsh, S.H. Wei, Crystal and electronic band structure of Cu2 ZnSn X4 (X=S and Se) photovoltaic absorbers: first-principles insights, Appl. Phys. Lett. 94 (2009), 041903, https://doi.org/10.1063/1.3074499.

[42] G. Sai Gautam, T.P. Senftle, E.A. Carter, Understanding the effects of Cd and Ag doping in Cu2ZnSnS4 solar cells, Chem. Mater. (2018), https://doi.org/10.1021/acs.chemmater.8b00677.

[43] J. Just, C.M. Sutter-Fella, D. Lützenkirchen-Hecht, R. Frahm, S. Schorr, T. Unold, Secondary phases and their influence on the composition of the kesterite phase in CZTS and CZTSe thin films, Phys. Chem. Chem. Phys. 18 (2016) 15988–15994, https://doi.org/10.1039/c6cp00178e.

[44] S. Schorr, G. Gurieva, M. Guc, M. Dimitrievska, A. Pérez-Rodríguez, V. Izquierdo-Roca, C.S. Schnohr, J. Kim, W. Jo, J.M. Merino, Point defects, compositional fluctuations, and secondary phases in non-stoichiometric kesterites, J. Phys. Energy. 2 (2019), 012002, https://doi.org/10.1088/2515-7655/ab4a25.

[45] Z.Y. Xiao, Y.F. Li, B. Yao, R. Deng, Z.H. Ding, T. Wu, G. Yang, C.R. Li, Z.Y. Dong, L. Liu, L.G. Zhang, H.F. Zhao, Bandgap engineering of Cu2CdxZn1-xSnS 4 alloy for photovoltaic applications: a complementary experimental and first-principles study, J. Appl. Phys. 114 (2013), https://doi.org/10.1063/1.4829457.

[46] U. Syafiq, N. Ataollahi, R. DiMaggio, P. Scardi, Solution-based synthesis and characterization ofcu2znsns4 (czts) thin films, Molecules (2019), https://doi.org/10.3390/molecules24193454.

[47] Q. Zhang, H. Deng, L. Chen, L. Yu, J. Tao, L. Sun, P. Yang, J. Chu, Cation substitution induced structural transition, band gap engineering and grain growth of Cu2CdxZn1−xSnS4thin films, J. Alloys Compd. 695 (2017) 482–488, https://doi.org/10.1016/j.jallcom.2016.11.121.

[48] J. Li, D. Wang, X. Li, Y. Zeng, Y. Zhang, Cation substitution in earth-abundant kesterite photovoltaic materials, Adv. Sci. (2018), https://doi.org/10.1002/advs.201700744.

[49] A.S. Bakri, M.Z. Sahdan, F. Adriyanto, N.A. Raship, N.D.M. Said, S.A. Abdullah, M. S. Rahim, Effect of annealing temperature of titanium dioxide thin films on structural and electrical properties, in: AIP Conf. Proc., AIP Publishing LLC AIP Publishing, 2017, 030030, https://doi.org/10.1063/1.4968283.

[50] S.K. Mishra, H. Roy, A.K. Lohar, S.K. Samanta, S. Tiwari, K. Dutta, A comparative assessment of crystallite size and lattice strain in differently cast A356 aluminium alloy, IOP Conf. Ser. Mater. Sci. Eng. (2015), https://doi.org/10.1088/1757-899X/75/1/012001.

[51] A. Sharmin, M.S. Bashar, M. Sultana, S.M.M. Al Mamun, Sputtered single-phase kesterite Cu2ZnSnS4 (CZTS) thin film for photovoltaic applications: post annealing parameter optimization and property analysis, AIP Adv. 10 (2020), 015230, https://doi.org/10.1063/1.5129202.

[52] H.A. Khawal, U.P. Gawai, K. Asokan, B.N. Dole, Modified structural, surface morphological and optical studies of Li 3+ swift heavy ion irradiation on zinc oxide nanoparticles, RSC Adv. 6 (2016) 49068–49075, https://doi.org/10.1039/C6RA04803J.

[53] A. Khare, B. Himmetoglu, M. Johnson, D.J. Norris, M. Cococcioni, E.S. Aydil, Calculation of the lattice dynamics and Raman spectra of copper zinc tin chalcogenides and comparison to experiments, J. Appl. Phys. 111 (2012), 083707, https://doi.org/10.1063/1.4704191.

[54] T. Tabaru, K. Shobu, M. Sakamoto, S. Hanada, Effects of substitution of Al for Si on the lattice variations and thermal expansion of Mo(Si,Al)2, Intermetallics 12 (2004) 33–41, https://doi.org/10.1016/j.intermet.2003.07.002.

[55] M. Kumar, A. Dubey, N. Adhikari, S. Venkatesan, Q. Qiao, Strategic review of secondary phases, defects and defect-complexes in kesterite CZTS-Se solar cells, Energy Environ. Sci. 8 (2015) 3134–3159, https://doi.org/10.1039/c5ee02153g.

[56] C. Persson, Electronic and optical properties of Cu2ZnSnS4 and Cu2ZnSnSe4, J. Appl. Phys. 107 (2010), 053710, https://doi.org/10.1063/1.3318468.

[57] C. Hu, F.E. Muller-Karger, R.G. Zepp, Absorbance, absorption coefficient, and apparent quantum yield: a comment on common ambiguity in the use of these optical concepts, Limnol. Oceanogr. (2002), https://doi.org/10.4319/lo.2002.47.4.1261.

[58] G. Rey, G. Larramona, S. Bourdais, C. Choné, B. Delatouche, A. Jacob, G. Dennler, S. Siebentritt, On the origin of band-tails in kesterite, Sol. Energy Mater. Sol. Cells 179 (2018) 142–151, https://doi.org/10.1016/j.solmat.2017.11.005.

[59] A. Sadeghzadeh-Attar, M.R. Bafandeh, Effect of annealing on UV-visible absorption and photoluminescence behavior of liquid phase deposited TiO2 nanorods, Int. J. Appl. Ceram. Technol. 16 (2019) 2429–2440, https://doi.org/10.1111/ijac.13271.

[60] R.S. Dubey, S. Saravanan, S. Kalainathan, Performance enhancement of thin film silicon solar cells based on distributed Bragg reflector & diffraction grating, AIP Adv. (2014), https://doi.org/10.1063/1.4904218.

[61] N.M. Ravindra, P. Ganapathy, J. Choi, Energy gap-refractive index relations in semiconductors - an overview, Infrared Phys. Technol. 50 (2007) 21–29, https://doi.org/10.1016/j.infrared.2006.04.001.

[62] What are dielectric materials? - properties, applications, Difference between Dielectric and Insulators and FAQs (n.d.), https://byjus.com/physics/dielectric-properties/. (Accessed 15 July 2021).

[63] Z.Y. Xiao, Y.F. Li, B. Yao, R. Deng, Z.H. Ding, T. Wu, G. Yang, C.R. Li, Z.Y. Dong, L. Liu, L.G. Zhang, H.F. Zhao, Bandgap engineering of Cu2CdxZn1-xSnS 4 alloy for photovoltaic applications: a complementary experimental and first-principles study, J. Appl. Phys. (2013), https://doi.org/10.1063/1.4829457.

[64] M.C. Rao, S.S. Basha, Structural and electrical properties of CZTS thin films by electrodeposition, Results Phys. (2018), https://doi.org/10.1016/j.rinp.2018.04.013.